Environmental Science & Technology

pubs.acs.org/est

Article

Ligand Coordination Directing High-Valent Iron-Oxo Reactivity for Pathway-Selective Pollutant Degradation

Xiaorong Yang, Qiongbin Zheng, Longsheng Wu, Jingping Hu,* Huijie Hou,* Guiying Li, Taicheng An, and Jiakuan Yang

Cite This: *Environ. Sci. Technol.* 2026, 60, 2728−2741

Read Online

ACCESS | Metrics & More | Article Recommendations | Supporting Information

ABSTRACT: The application of high-valent iron-oxo species for the degradation of organic contaminants is a promising strategy. However, the role of the catalyst's coordination sphere in regulating the reaction mechanism remains ambiguous. Here, we elucidate this structure−reactivity relationship by deploying three iron porphyrins with strategically varied ligand substitutions to activate H_2O_2 for bisphenol A (BPA) degradation. We demonstrate that the ligand coordination of the catalyst directs the nature of the generated Fe^{IV}-oxo species, the identity of the cogenerated radicals, and the pollutant degradation pathways. Specifically, the *β*-substituted catalyst exclusively generates the Fe^{IV}═O unit with a ligand *π*-cation radical, transforming BPA to hydroxylation products via an oxygen adduct formation pathway with strong matrix tolerance. Conversely, meso-substituted catalysts generate protonated Fe^{IV}−OH species and coexisting oxygen-centered radicals. Meso-carboxyl substitution yields (por)Fe^{IV}−OH and $HO^{\bullet}$, which synergistically induce ring cleavage of BPA through a single-electron-transfer (SET)-initiated attack. Meso-sulfoxyl substitution produces $[(por)Fe^{IV}-OH]^{+}$ and $HO_2^{\bullet}$, which drive quinonization of BPA via a coupled SET and hydrogen-atom-abstraction mechanism. These findings reveal that the coordination environment of the catalyst critically modulates the protonation state and reactivity of the generated high-valent iron-oxo species, thereby steering pollutant degradation toward pathway-selective transformations. This work provides fundamental mechanistic insights into the targeted detoxification of organic compounds.

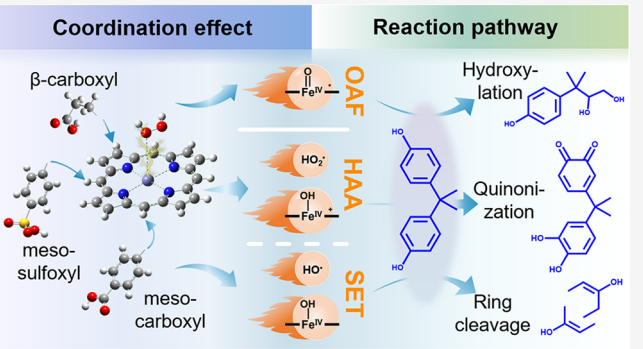

KEYWORDS: *high-valent iron-oxo species, coordination environment, reaction mechanism, pathway-selective degradation, molecular orbital, iron porphyrin*

1. INTRODUCTION

Advanced oxidation processes (AOPs) represent a promising array of treatment technologies for remediating recalcitrant organic pollutants, possessing excellent removal efficiency, remarkable adaptability, and technical versatility.[1−3] The conventional AOPs rely on the generation of nonselective radicals to eliminate pollutants, such as hydroxyl radicals ($HO^{\bullet}$), sulfate radicals ($SO_4^{\bullet-}$), and super oxygen radicals ($O_2^{\bullet-}$).[4−6] However, these radicals are often hampered in practical applications by scavenging from background water matrices,[7−9] which diminishes their efficiency against micropollutants. This limitation has stimulated interest in alternative oxidants, such as high-valent metal-oxo species, which offer greater selectivity and stability for targeted wastewater treatment.[10,11]

High-valent iron-oxo species have garnered increasing interest due to their strong oxidizing capacity, diverse reaction pathways, and longer lifetimes.[12−14] High-valent iron-oxo species are among the most potent oxidants known in nature,[15] which have been extensively investigated in biomimetic models and enzymatic systems, such as cytochromes P450 and peroxidases with Fe/N_4−C structures.[16−18] It is well established that the primary oxidant in these enzymes typically exists with Fe^{IV}═O unit coupled to porphyrin *π*-cation radical ($(por)^{\bullet+}Fe^{IV}$═O, Compound I),[19] and its reactivity pattern follows well-established hydrogen-atom-abstraction (HAA) and oxygen-rebound pathways.[20,21] The reactivity and selectivity of high-valent iron-oxo species are intimately governed by their local coordination environment. Several works have highlighted that ligand perturbations, such as the introduction of electron-withdrawing substituents, heteroleptic ligand architectures, or asymmetric equatorial environments on porphyrin or phthalocyanine macrocycles,

Received: July 27, 2025
Revised: December 9, 2025
Accepted: January 5, 2026
Published: January 9, 2026

https://doi.org/10.1021/acs.est.5c10288
Environ. Sci. Technol. 2026, 60, 2728−2741

can dramatically tune the oxidizing power and selectivity of high-valent iron-oxo species.[22−24] Furthermore, Shaik and coworkers have pioneered the concept of electric-field effects, revealing that charged substituents in the coordination sphere generate a directional electric field.[25−27] These electric fields stabilize specific electronic states and modulate reaction barriers by lowering the energy of electron-acceptor orbitals.[28−30] In the past 2 years, studies based on Fe/Nx-C structures have revealed that reducing the electron density of the central iron through coordination-field effects can strengthen the Fe−N bond and feature stronger peroxide adsorption affinity, facilitating the generation of Fe^{IV}=O species and enhancing catalytic durability.[31,32] These insights form the foundation for catalyst design strategies that exploit subtle ligand and electronic modifications to control reactivity.

One of the outstanding applications of these insights is the synthesis of single-atom catalysts (SACs) with Fe/Nx-C structure,[33,34] which can maximize atomic utilization and exhibit unique reactivity for environmental remediation.[35,36] It is well documented that organic substrates can be oxidized into hydroxylated, epoxidated, or quinone products in the reaction catalyzed by Fe/Nx-C complexes, where high-valent iron-oxo species are the key oxidative intermediates.[37−39] Nevertheless, current research has primarily focused on catalyst design for oxidant activation, pollutant degradation efficiencies, and product analysis.[32,40,41] Despite the widespread recognition that the coordination environment regulates catalytic activity, the mechanistic role of the coordination environment in defining the electronic configuration and directing the reaction pathway of high-valent iron-oxo species has remained poorly understood in the field of materials catalysis. Extensive studies have elucidated the metabolic activation of bisphenol A (BPA) by the P450 enzymes. Interestingly, while the key oxidant is consistently the high-valent iron-oxo species, the degradation products vary significantly depending on the biological source. For instance, human hepatic P450s primarily induce aromatic hydroxylation,[42] whereas certain microbial or plant P450s facilitate oxidative rearrangement or cleavage.[43,44] These divergences suggest that the local environment of the heme cofactor plays a decisive role in tuning the reaction product. However, disentangling these environmental factors within the complex protein matrix remains experimentally challenging. This underscores the need for well-defined biomimetic models to unravel structure−reactivity relationships.

Iron porphyrins are particularly attractive as homogeneous biomimetic catalysts with Fe/N_4−C structure, serving as well-defined molecular analogues of cytochrome P450 enzymes.[45] The tunable molecular structure of porphyrins allows for precise and systematic modification of the coordination environment to isolate the effects of ligand isomerism (β- vs meso-site) and electronic tuning, offering a level of control that is unattainable with heterogeneous SAC catalysts or complex P450 enzyme systems, thus making them an ideal platform to deconstruct the structure−reactivity relationship of high-valent iron-oxo species. Recent computational studies revealed energetically feasible pathways for $(por)^{\bullet+}Fe^{IV}$=O-mediated BPA hydroxylation and aromatic-ring activation through theoretical calculations on human CYP 2C9,[46] which establish an important biochemical and computational foundation for understanding how high-valent iron-oxo species react with substrates. Our previous work highlighted that the substituent position on iron porphyrins (β-site and meso-site) dictates the catalytic behavior in organic pollutant degradation,[47,48] but the underlying reaction mechanisms and the precise role of the coordination environment in governing the interaction between active species and pollutants remained unresolved. The present study fills this critical gap through a synergistic experimental and in-depth theoretical approach.

In this study, three types of iron porphyrins with distinct ligands were used to activate H_2O_2 for the degradation of BPA, a model pollutant due to its environmental relevance, amphiphilic electronic structure, and well-documented degradation pathways that allow for clear mechanistic analysis. To further assess the generality of the catalytic behavior, several representative phenolic pollutants were also examined. This work provides the systematic and comparative demonstration that ligand isomerism (β- vs meso-site) and electronic tuning (carboxyl vs sulfoxyl) of the coordination environment can be strategically employed to control the formation of distinct high-valent iron-oxo/radical groups within a tunable homogeneous catalytic platform, rather than within complex protein matrices. By combining kinetic studies, active species and product identification, and deep molecular-level insights from density functional theory (DFT) calculations, we establish a predictive roadmap linking catalyst structure to the nature of the generated Fe^{IV}-oxo species, the identity of the cogenerated radicals, and the pollutant degradation pathways. For the first time, this study uses a precisely defined homogeneous system to reveal how specific ligand placements and electronic properties control the nature and reactivity of the active Fe^{IV}-oxo species, providing transferable mechanistic insights that may inspire rational coordination design in environmental oxidation catalysis for pathway-selective pollutant degradation.

2. MATERIALS AND METHODS

2.1. Chemicals

All chemical reagents were used as received (Text S1). Three types of iron porphyrins with distinct ligand environments, including Fe(III) chlorophyll (ChlFe, β-carboxyl substitution), Fe(III) meso-tetra(4-carboxyphenyl)porphine chloride (TCPFe, meso-carboxyl substitution), and Fe(III) meso-tetra(4-sulfophenyl)porphine chloride (TSPFe, meso-sulfoxyl substitution), were employed for BPA degradation. The schematic molecular structures of these catalysts are provided in Figure S1.

2.2. Experimental Procedures

Iron porphyrin stock solutions with a concentration of 1 mM were prepared using ultrapure water and quantified by Inductively Coupled Plasma Optical Emission Spectroscopy after acid digestion. The experiments on H_2O_2 activation by iron porphyrin for phenolic pollutants degradation were carried out in a 100 mL conical flask under constant magnetic stirring at ambient temperature (25 ± 0.5 °C) and pressure. In a typical reaction, the iron-porphyrin stock solution was mixed with the phenolic contaminant stock solution, and ultrapure water was added to achieve a total volume of 39 mL, yielding a final catalyst concentration of 0.02−0.12 mM, depending on the system studied. The initial pH value of the solution was adjusted using NaOH (0.1 M) or HCl (0.05 M) and measured with a pH meter (Sartorius PB-10, Germany). The oxidation reaction was initiated by introducing H_2O_2. During the reaction, 1 mL of solution was quickly sampled from the reactor at certain time intervals, in which 0.3 mL of 0.8 M Na_2SO_3 solution was preinjected to quench the reaction. Samples were filtered through a 0.22 μm PVDF membrane

https://doi.org/10.1021/acs.est.5c10288
Environ. Sci. Technol. 2026, 60, 2728−2741

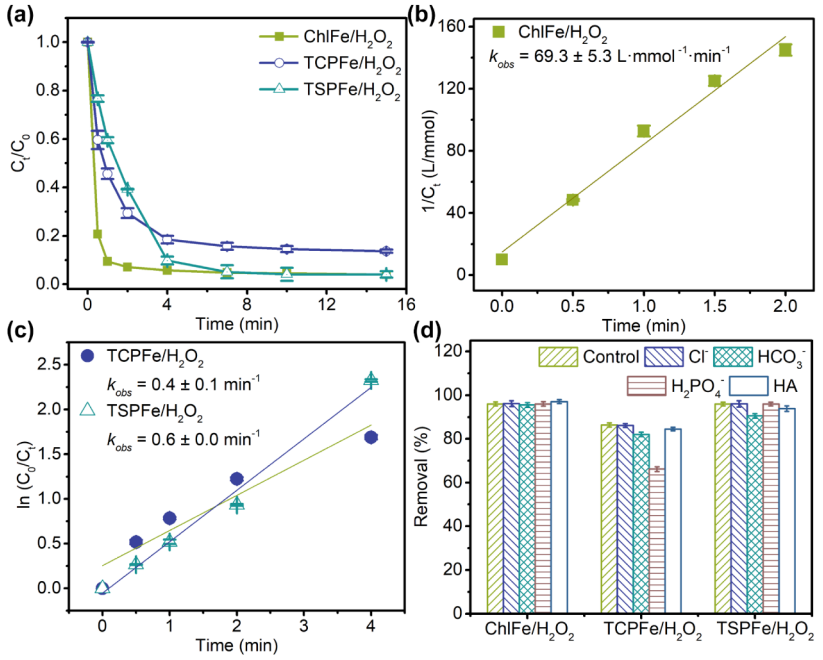

Figure 1. Degradation behaviors of BPA in iron-porphyrin/H_2O_2 systems. (a) BPA degradation profiles in iron-porphyrin/H_2O_2 systems. (b) Pseudo-second-order kinetics in ChlFe/H_2O_2 system. (c) First-order kinetics in TCPFe/H_2O_2 and TSPFe/H_2O_2 systems. (d) Effect of various matrices on BPA degradation in iron porphyrin/H_2O_2 systems. Initial experimental conditions: ChlFe = 0.12 mM, H_2O_2 = 5 mM, BPA = 0.1 mM, pH = 9 in the ChlFe/H_2O_2 system; TCPFe = 0.02 mM, H_2O_2 = 4 mM, BPA = 0.3 mM, pH = 7.5 in the TCPFe/H_2O_2 system; TSPFe = 0.02 mM, H_2O_2 = 4 mM, BPA = 0.3 mM, pH = 4 in the TSPFe/H_2O_2 system. Cl^- = 5 mM, HCO_3^- = 5 mM, $H_2PO_4^-$ = 5 mM, and HA = 20 mg/L.

prior to analysis. The solution pH was monitored and confirmed to remain nearly constant throughout the reaction. All experiments were performed in triplicate, and the results are presented as means with standard deviations shown as error bars.

2.3. Computational and Analytical Methods

The computational and analytical methods and details are listed in Text S2.

3. RESULTS AND DISCUSSION

3.1. Degradation Kinetics of BPA by Catalysts with Different Ligand Coordination

The catalytic activity of the three-iron porphyrin/H_2O_2 systems for BPA degradation was evaluated (Figure 1a). All systems achieved efficient BPA removal within minutes, but their kinetic profiles differed significantly. The ChlFe/H_2O_2 system, featuring a β-carboxyl substituent, exhibited the fastest degradation, following pseudo-second-order kinetics (R^2 = 0.977) with a rate constant (k_{obs}) of 69.3 L·mmol^{-1}·min^{-1} (Figure 1b). For comparison, a pseudo-first-order fitting was also performed (Figure S2), but it yielded a poorer correlation (R^2 = 0.731). In contrast, the meso-substituted TCPFe and TSPFe systems both followed pseudo-first-order kinetics, with k_{obs} values of 0.4 min^{-1} and 0.6 min^{-1}, respectively (Figure 1c). In addition, the introduction of typical matrices that are omnipresent in environmental waterbodies showed only minor influences on BPA degradation. Specifically, the ChlFe/H_2O_2 system maintained nearly unchanged removal efficiency, whereas TCPFe/H_2O_2 and TSPFe/H_2O_2 systems showed slightly lower degradation rates in the presence of HCO_3^- and HA, and the addition of $H_2PO_4^-$ significantly hindered BPA removal due to the acidification of the solution in the TCPFe/H_2O_2 system (Figure 1d). This comparison highlights that the β-substituted ChlFe catalyst possesses a higher matrix tolerance than the meso-substituted analogues. These divergences point to fundamental differences in the BPA degradation mechanisms between β- and meso-substituted porphyrins.

The UV−vis spectra of the three iron porphyrins exhibit a similar Soret band at ∼400 nm and Q-bands at 500−700 nm, but variations in their substituent groups induce slight shifts in the characteristic absorption bands (Figure S3a). By observing the changes in Soret band intensity and H_2O_2 concentration, distinct trends were obtained between the β-position porphyrin system and the meso-position porphyrin systems. In the ChlFe/H_2O_2 system, a large quantity of H_2O_2 was consumed (Figure S3b), whereas ChlFe showed less attenuation, with a high initial rate in the intensity of its Soret band (Figure S3c), indicating a more efficient catalytic cycle of the homogeneous ChlFe catalyst. The fastest H_2O_2 consumption rate was observed in the meso-carboxyl-substituted TCPFe/H_2O_2 system, which is consistent with DFT analysis revealing the lowest energy barrier required for the O−O bond cleavage in H_2O_2 activation by TCPFe, according to transition state theory (Figure S3d).[49] While the k_{obs} values of 0.4 min^{-1} was the lowest, indicating that more complex elementary reactions are involved for BPA degradation in the TCPFe/H_2O_2 system. Although H_2O_2 was rarely consumed in meso-substituted porphyrin systems (Figure S3b), the intensity of the Soret band of the iron porphyrins exhibited significant attenuation (Figure S3c). This phenomenon may be attributed to the absence of reaction substrates, where homogeneous iron porphyrin is oxidized instead, implying the presence of strongly oxidizing species in the meso-substituted porphyrin systems. These observations collectively establish the distinct activation behaviors of

https://doi.org/10.1021/acs.est.5c10288
Environ. Sci. Technol. 2026, 60, 2728−2741

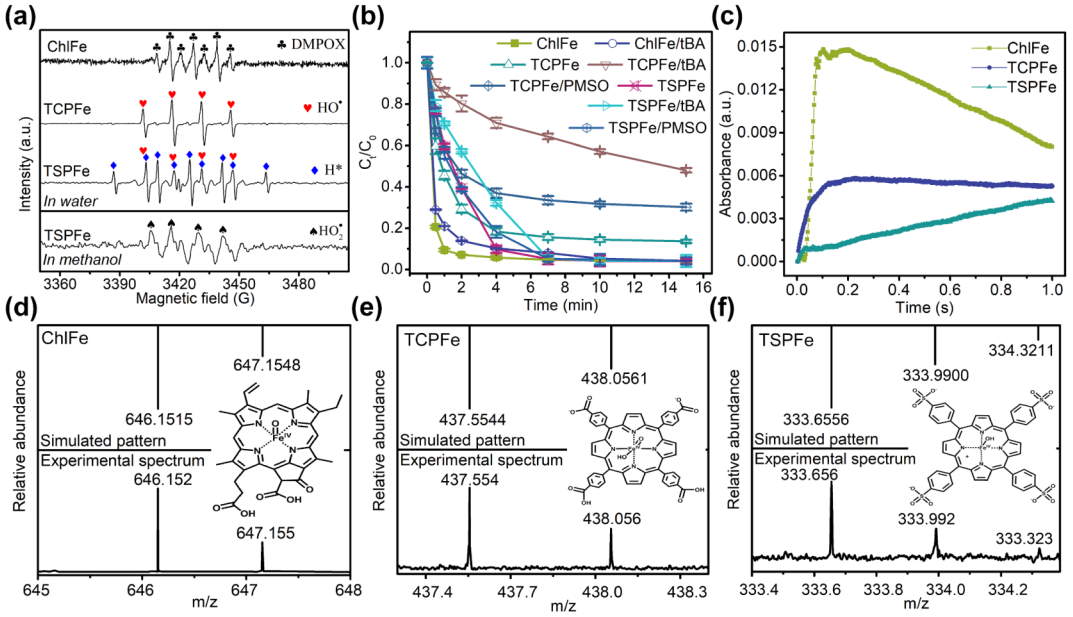

Figure 2. Identification of active species in iron-porphyrin/H_2O_2 systems. (a) DMPO-trapped EPR spectra of iron-porphyrin/H_2O_2 systems in aqueous or methanol solution. (b) BPA degradation profile in iron-porphyrin/H_2O_2 systems with the addition of different scavengers. (c) Temporal absorbance variations at 590 nm of iron porphyrins and the H_2O_2 mixture during the reaction process. ESI-FTMS spectra of mixtures of (d) ChlFe, (e) TCPFe, and (f) TSPFe were recorded with H_2O_2. Initial experimental conditions: ChlFe = 0.12 mM, BPA = 0.1 mM, H_2O_2 = 5 mM, pH = 9 in the ChlFe/H_2O_2 system; TCPFe = 0.02 mM, BPA = 0.3 mM, H_2O_2 = 4 mM, pH = 7.5 in the TCPFe/H_2O_2 system; TSPFe = 0.02 mM, H_2O_2 = 4 mM, BPA = 0.3 mM, pH = 4 in the TSPFe/H_2O_2 system; PMSO = 200 μM, tBA = 1.3 M.

catalysts, modulated by ligand coordination, for BPA degradation.

To further assess whether the ligand coordination-dependent kinetic behavior observed for BPA degradation is generalizable to other phenolic pollutants, additional degradation experiments were performed using phenol and TCP under identical catalytic conditions. Similar ligand coordination-dependent degradation kinetics were observed among different organic contaminants (Figure S4). In addition, there were differences in the degradation efficiency of different pollutants and the selectivity of different catalytic systems. The ChlFe catalyst exhibited pronounced selectivity, rapidly and preferentially degrading BPA, while phenol and TCP were less reactive (Figure S4a). The meso-substituted TCPFe and TSPFe exhibited a broader but less selective oxidation behavior (Figure S4b,c). These divergences are caused not only by the ligand coordination effect of the catalyst but also by the intrinsic electronic structures and substituents of the pollutants themselves. These observations confirm that ligand coordination not only regulates the formation of distinct active species but also governs substrate selectivity toward diverse pollutants. The consistency of degradation kinetics across different substrates highlights the generality of the proposed structure−reactivity mechanism.

3.2. Ligand Coordination Control of the Generation of Distinct Active Species

It should be noted that the optimal pH values (9.0 for ChlFe, 7.5 for TCPFe, and 4.0 for TSPFe) were chosen to achieve the highest catalytic efficiency. Although variations in pH may influence the speciation and protonation state of the Fe center, these effects are inherently associated with the intrinsic coordination characteristics of the respective ligands. Therefore, the main focus of this study is the fundamental role of ligand coordination effects. Distinct active species were identified in different iron porphyrin/H_2O_2 systems. EPR spectra of DMPO-trapped radicals reveal the generation of distinct reactive species in each system (Figure 2a). In the ChlFe/H_2O_2 system, the EPR signal corresponding to DMPOX indicates the presence of a powerful oxidant, while the absence of the characteristic DMPO−OH adduct and tBA quenching experiments rules out free hydroxyl radicals (Figure 2b). The sharp increase in the Q-band absorbance of ChlFe within the first 100 ms of the reaction indicates the formation of Fe^{IV}-oxo porphyrin (Figure 2c).[50] ESI-FTMS analysis was performed to further characterize the active species, revealing a species at m/z 646.152 that corresponds to the oxygen adduct of ChlFe (Figure 2d), denoted as $(Chl)^{\bullet+}Fe^{IV}{=}O$.[48] Given that $Fe^{IV}{=}O$ species react with PMSO to form phenyl methyl sulfone ($PMSO_2$), whereas other radicals transform PMSO into hydroxylated products, PMSO is widely recognized as a well-established probe for $Fe^{IV}{=}O$ species.[14] The temporal variation of PMSO and $PMSO_2$ concentrations confirms that this $Fe^{IV}{=}O$ species dominates the oxidation pathway in the ChlFe/H_2O_2 system (Figure S5a). This result further confirms the predominant role of $(Chl)^{\bullet+}Fe^{IV}{=}O$ in the ChlFe/H_2O_2 system.

Conversely, the meso-substituted iron porphyrin systems generated a mixture of species. The TCPFe/H_2O_2 system produced characteristic EPR signals for DMPO−$HO^{\bullet}$ (Figure 2a), confirming the generation of $HO^{\bullet}$. Scavenging experiments with tBA partially inhibited BPA degradation, further supporting the role of $HO^{\bullet}$ but also implying the presence of other tBA-resistant species (Figure 2b). The absorbance changes in the Q-band of TCPFe during the initial reaction stage revealed the formation of the Fe^{IV}-oxo porphyrin (Figure 2c). ESI-FTMS revealed a species at an m/z of 437.554 (Figure 2e), which is consistent with the isotope distribution patterns of the oxygen adduct of TCPFe ($(por)Fe^{IV}{=}O$) with two negative charges. Although PMSO was extensively

https://doi.org/10.1021/acs.est.5c10288
Environ. Sci. Technol. 2026, 60, 2728−2741

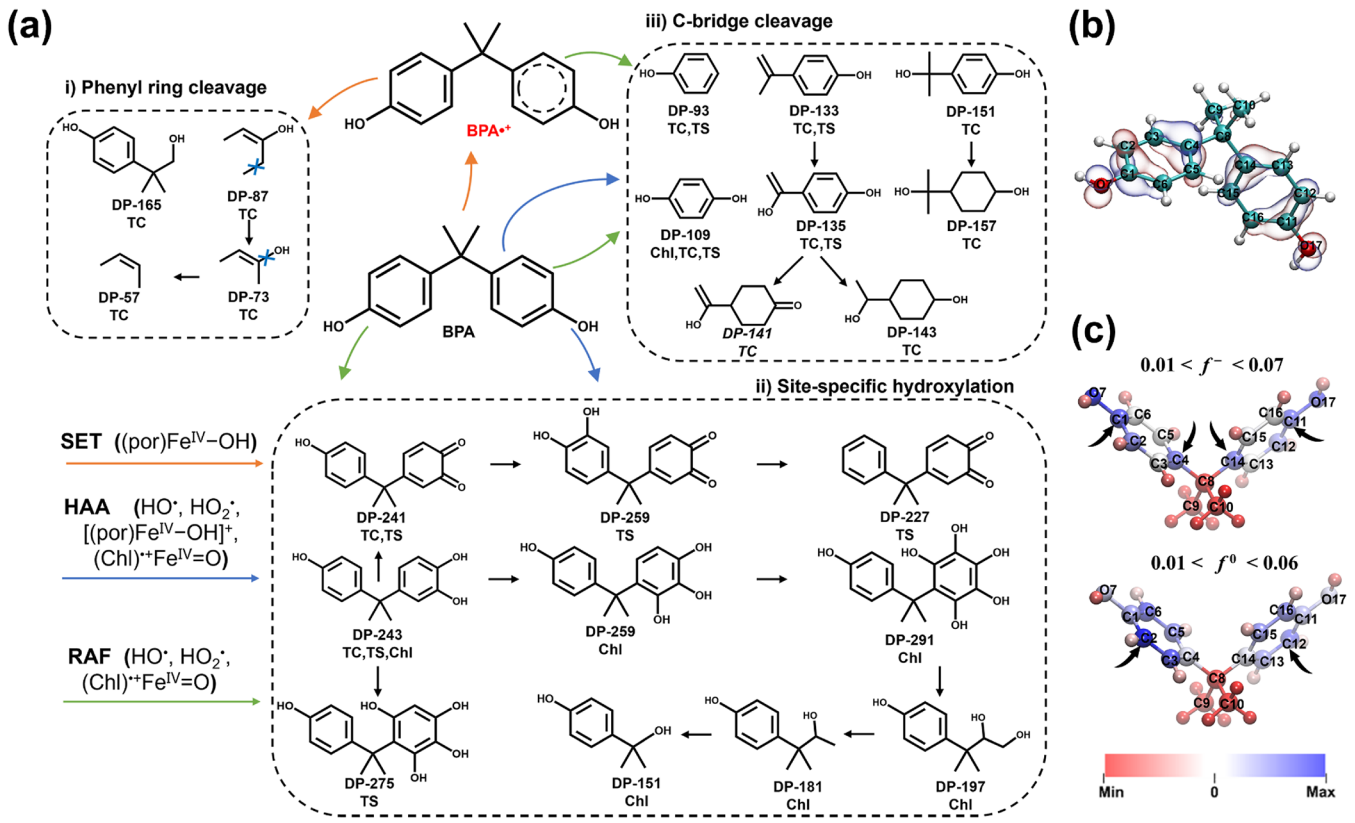

Figure 3. Degradation pathway and reactive site prediction of BPA. (a) BPA degradation pathway in iron-porphyrin/H_2O_2 systems. (b) HOMO of BPA. (c) Condensed Fukui index of BPA.

consumed in the TCPFe/H_2O_2 system, negligible sustained generation of $PMSO_2$ was observed (Figure S5b), indicating that the presence of the (por)Fe^{IV}=O species is extremely limited. Upon the introduction of tBA, the consumption of PMSO was significantly reduced (Figure S5b), suggesting that PMSO degradation in the TCPFe/H_2O_2 system is primarily mediated by $HO^•$. However, both tBA and PMSO did not completely inhibit BPA degradation in the TCPFe/H_2O_2 system (Figure 2b), implying the existence of other reactive species. This phenomenon is aligned with our previous inference, where (por)Fe^{IV}=O is the precursor to the active Fe^{IV}–OH species, (por)Fe^{IV}–OH.[47] Therefore, (por)Fe^{IV}–OH species is not directly detected but is inferred as the most logical candidate based on the above constellation of indirect evidence.

The TSPFe/H_2O_2 system, with strongly electron-withdrawing sulfoxyl groups at the meso-position, exhibited EPR signals for DMPO-H* in aqueous solution and DMPO- $HO_2^•$ adducts in methanol (Figure 2a). These $HO_2^•$ radicals reversibly equilibrate with their conjugate base $O_2^{•-}$ as the p*Ka* is 4.8 under experimental pH conditions.[51] It is well-known that tBA also has H* scavenging capacity[52] and pBQ could selectively block $O_2^{•-}$ participation in BPA degradation with a high reaction rate ($k_{O2•-/pBA}$ = 1.0 × 10^9 $M^{-1}s^{-1}$).[51] The addition of pBQ notably retarded BPA degradation during the initial stage of the reaction (Figure S5c). The Q-band absorbance changes of TSPFe during the reaction manifested the formation of the Fe^{IV}-oxo porphyrin (Figure 2c). The PMSO probe experiment similarly indicates that Fe^{IV}-oxo does not exist in the Fe^{IV}=O form (Figure S5d). More importantly, ESI-FTMS detected a species with an *m*/*z* shifting from 327.989 to 338.656 following the addition of H_2O_2 (Figure S6 and Figure 2f), which is consistent with the isotope distribution of a cationic iron-hydroxo complex, i.e., [(por)-Fe^{IV}–OH]$^+$. The BPA degradation was largely unaffected by the addition of PMSO but was almost completely suppressed by ABTs (Figure S5c), a probe for electron-transfer pathways, confirming that a nonradical electron-transfer mechanism dominates the overall process in the TSPFe/H_2O_2 system.

In summary, the coordination environment of the iron porphyrin catalyst indicates the protonation state of the Fe^{IV}-oxo species and the generation of radicals. The *β*-substituted ChlFe exclusively produces (Chl)$^{•+}Fe^{IV}$=O. The meso-carboxyl-substituted TCPFe cogenerates (por)Fe^{IV}–OH and $HO^•$. The meso-sulfoxyl-substituted TSPFe cogenerates [(por)Fe^{IV}–OH]$^+$ and $HO_2^•$. These distinct groups of active species are responsible for the observed differences in degradation kinetics. Therefore, due to variations in the ligand coordination of iron porphyrin catalysts, different forms of Fe^{IV} species are generated. Furthermore, oxygen-centered radicals are also produced in meso-substituted iron porphyrin systems, coexisting with Fe^{IV}-oxo species. Extensive research has been conducted on the coordination effects influencing the activation of peroxides by iron-based catalysts to generate high-valent iron-oxo species.[53−55] However, the influence of the coordination environment on the reactivity of the generated high-valent iron-oxo species and their reaction mechanisms with contaminants remains poorly understood. In this study, the reactivity of different forms of Fe^{IV}-oxo species with distinct ligand coordination, as well as their reaction mechanisms with BPA, are systematically investigated.

https://doi.org/10.1021/acs.est.5c10288
Environ. Sci. Technol. 2026, 60, 2728−2741

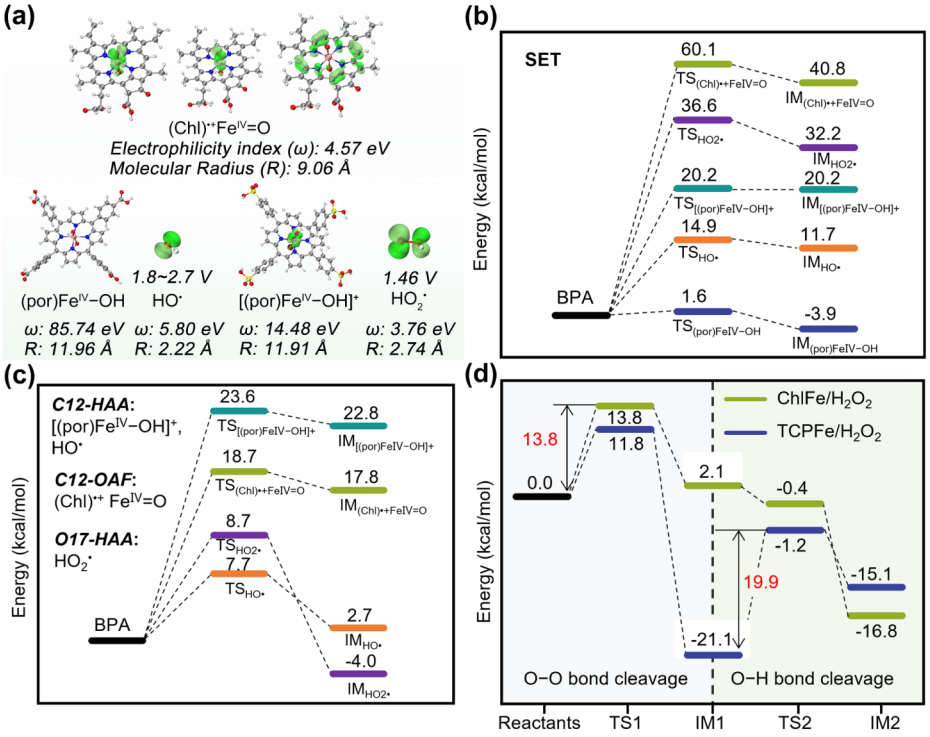

Figure 4. Reactivities of distinct active species and relevant reaction energy profiles. (a) The SOMOs and reactivity characteristics of $(Chl)^{\bullet+}Fe^{IV}$═O in the $ChlFe/H_2O_2$ system, $(por)Fe^{IV}$−OH and $HO^{\bullet}$ in the $TCPFe/H_2O_2$ system, $[(por)Fe^{IV}-OH]^+$ and $HO_2^{\bullet}$ in the $TSPFe/H_2O_2$ system. Schematic free energy diagram of the initial elementary reaction for BPA oxidation by active species with the (b) SET route, (c) HAA route at the C12 site, HAA route at the O17 site, and the OAF route at the C12 site. (d) The energy barrier during the activation of H_2O_2 by iron-porphyrins.

3.3. Different Reaction Mechanisms of Active Species with BPA

Diverse types of BPA degradation products (DPs) have been identified by U-HPLC-Q-Exactive Orbitrap HRMS in these iron porphyrin/H_2O_2 systems (Table S1). These products generally exhibit significantly lower endocrine-disrupting potency and estrogen receptor binding affinity compared with BPA, as reported in previous studies.[56,57] According to QSAR calculations,[58,59] the bioconcentration factors of these DPs are all lower than that of the parent BPA. Furthermore, the lethal concentration 50% (LC_{50}) for *Daphnia magna* increased in all cases (Figure S7), which indicates that the toxicity of BPA is decreased or even eliminated through degradation by iron porphyrin systems. The BPA degradation can be proposed into three distinct pathways (Figure 3a): (i) The first pathway involves the hydroxylation of BPA, which typically occurs in the $ChlFe/H_2O_2$ system. (ii) The second pathway forms products involving cleavage of isopropyl bridges or ring-opening of phenol moieties, primarily observed in the $TCPFe/H_2O_2$ system. (iii) The third pathway entails the quinonization of BPA, predominantly found in the $TSPFe/H_2O_2$ system.

Analysis of BPA's electronic structure revealed that its highest occupied molecular orbital (HOMO) is localized on the π-conjugated benzene rings (Figure 3b), rendering them susceptible to electrophilic attack. The condensed Fukui index effectively identified the active atoms (Table S2). C4 ($f^- = 0.057$) and C14 ($f^- = 0.058$) show the highest propensity for electrophilic attack, attributed to their higher f^- values and minimal Δf indices, while C2 ($f^0 = 0.061$) and C12 ($f^0 = 0.059$) demonstrate potential for radical targeting (Figure 3c). The hydrogen atoms bonded to C2, C12, and O17 are the most reactive sites for electrophilic attack because of their higher condensed f^- values among all hydrogen atoms (Table S3). The symmetric structure of BPA molecules, therefore, prompted an in-depth analysis of C12, C14, and O17 as putative active sites for active species attack.

The active species responsible for BPA degradation exhibit distinct chemical reactivities. The electronic characteristics of these active species can be quantified through single-occupied molecular orbital (SOMO) distributions and electrophilicity indices (ω). In the $ChlFe/H_2O_2$ system, $(Chl)^{\bullet+}Fe^{IV}$═O possesses three SOMOs (Figure 4a), which could promote hydrogen atom abstraction followed by oxygen rebound mechanism to realize oxygen adduct formation (OAF).[60] $(por)Fe^{IV}$−OH exhibits higher electron affinity (ω = 85.74 eV) (Figure 4a), which could oxidize the substrate through single electron transfer (SET). The cationic $[(por)Fe^{IV}-OH]^+$ shows a radical character (localized SOMO) and high electrophilicity (Figure 4a), enabling dual reaction pathways: SET and HAA. Comparatively, oxygen-centered radicals ($HO^{\bullet}$ and $HO_2^{\bullet}$) exhibit high redox potential (1.8 ~ 2.7 V for $HO^{\bullet}$[52] and 1.46 V for $HO_2^{\bullet}$[61]), enabling synergistic interaction with coexisting Fe^{IV}-oxo species to achieve complete degradation of BPA. Furthermore, they can exploit their respective radical properties and small radius to oxidize substrates via HAA and OAF mechanisms (Figure 4a).

The elementary reaction between BPA and active species can proceed through three mechanisms: SET, HAA, and OAF. The calculated free energy diagrams of each initial elementary reaction at specific reactive sites are shown in Figure 4b,c. The feasibility of a reaction can be determined by calculating the corresponding reaction rate constant by using the activation energy barrier. The protonated species, $(por)Fe^{IV}$−OH and

https://doi.org/10.1021/acs.est.5c10288
Environ. Sci. Technol. 2026, 60, 2728−2741

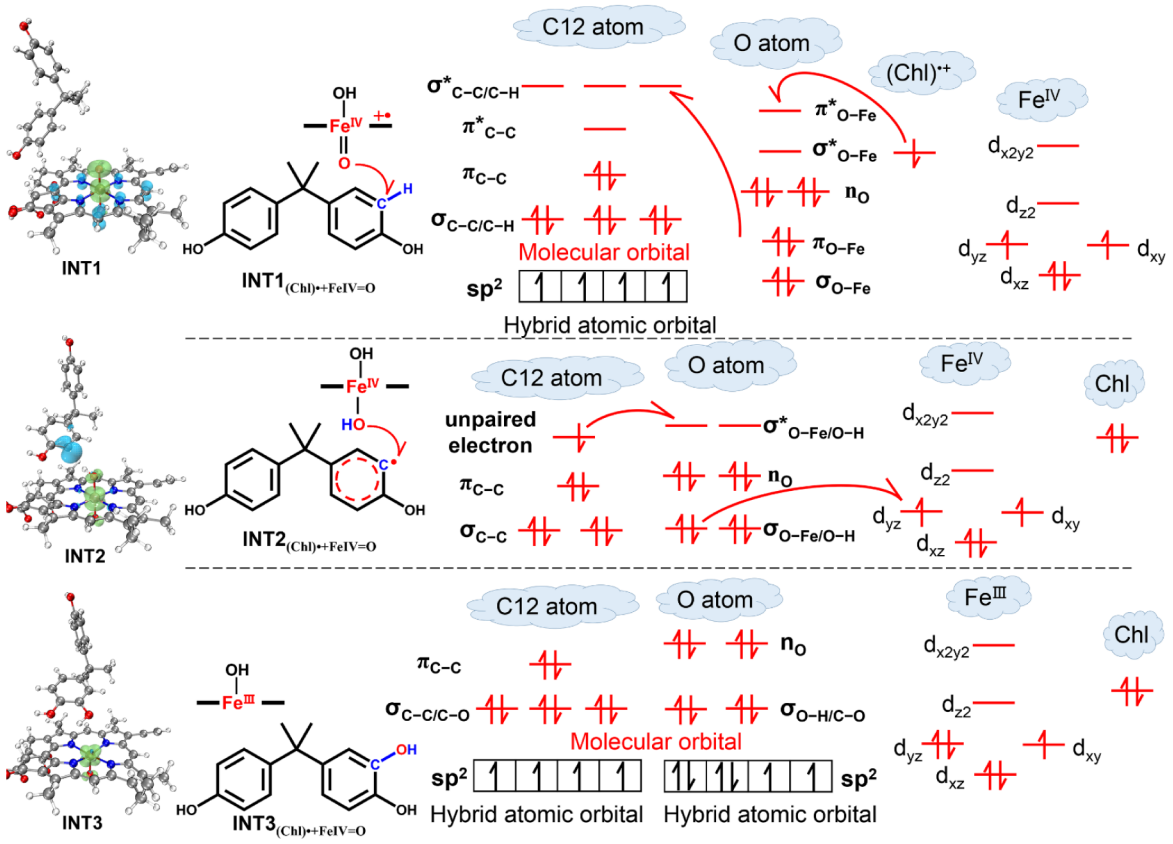

Figure 5. Distribution of the spin density and the mechanism of the OAF reaction for BPA degradation by $(Chl)^{\bullet+}Fe^{IV}$=O at C12. C12−H bond cleavage resulted from HAA initiated by the radical character of the chlorin ring to form the Fe^{IV}−OH species and BPA radical. Then Fe^{IV}−OH transfers the OH group back to the BPA radical, yielding hydroxylated BPA and ChlFe.

$[(por)Fe^{IV}-OH]^+$, exhibit Fe−O bond lengths of 1.815 Å and 1.821 Å, respectively (Table S4), which align perfectly with the typical range (1.81−1.84 Å) for protonated Compound II.[62,63] The negligible barrier of 1.6 kcal/mol and the Fe−O bond elongation to 1.913 Å support an efficient SET mechanism for the $(por)Fe^{IV}-OH$ species generated in the TCPFe/H_2O_2 system (Figure 4b). This facile SET process is rationalized by the electric field effect induced by the meso-charged groups.[64] Although $[(por)Fe^{IV}-OH]^+$ exhibits a relatively high activation energy barrier ($\Delta G^{\ddagger}$ = 20.2 kcal/mol) for BPA degradation via the SET pathway, a reaction rate constant of 0.58 min^{-1} and a BPA degradation half-life of 1.2 min were calculated based on first-order kinetics through transition state theory.[65] These theoretical values show excellent agreement with experimental observations (Figure 1a,c), confirming that BPA degradation by $[(por)Fe^{IV}-OH]^+$ through the SET pathway remains viable. In contrast, significantly higher activation energy barriers associated with the $SET_{HO2\bullet}$ and $SET_{(Chl)\bullet+FeIV=O}$ pathways indicate that these alternative pathways are kinetically unfavorable. The detailed analysis of reaction energy and kinetic parameters is provided in Text S3. By analogous reasoning, transition states were identified for the HAA pathway at the C12 site via $HO^{\bullet}$ and at the O17 site via $HO_2^{\bullet}$, as well as for the OAF pathway at the C12 site via $(Chl)^{\bullet+}Fe^{IV}$=O (Figure 4c), and these reactions are calculated to be kinetically feasible. The contradiction between the higher calculated activation energy barrier for BPA activation and the faster observed degradation rate of BPA in the ChlFe/H_2O_2 system was discussed and explained in Text S4 (Figure 4d).

3.4. Selective hydroxylation via OAF Pathway in the ChlFe/H_2O_2 System

The BPA degradation proceeds through an OAF pathway mediated by $(Chl)^{\bullet+}Fe^{IV}$=O in the ChlFe/H_2O_2 system. Prior to the reaction, spin density is primarily localized on the axial Fe=O moiety and the porphyrin ring (Figure 5). The bonding molecular orbitals of the active O atom consist of one σ_{Fe-O} orbital, one π_{Fe-O} orbital, and two n_O orbitals. Notably, the $(Chl)^{\bullet+}Fe^{IV}$=O species characterized here exhibits an Fe=O bond length of 1.658 Å and a spin density distribution consistent with an Fe^{IV}=O center coupled to a porphyrin radical, which matches the benchmark range (1.64−1.69 Å) and electronic descriptions reported for Compound I.[46,66] The ChlFe system promotes BPA degradation via the OAF pathway to yield hydroxylated products. During the reaction, the Fe=O bond elongates from 1.658 Å to 1.799 Å, which matches the geometric characteristics of H-abstraction transition states, and the subsequent elongation to 3.589 Å signifies the completion of oxygen transfer (Table S4).[67] The calculated barrier for the direct aromatic hydroxylation of BPA by $(Chl)^{\bullet+}Fe^{IV}$=O (18.7 kcal/mol) is slightly higher than that of direct aromatic hydroxylation (12−17 kcal/mol) and the energy barrier for P450 metabolism of BPA (16.3 or 17.6 kcal/mol).[46,68] These differences are chemically reasonable, given the larger steric hindrance of BPA and the distinct coordination environments of the Fe=O unit. The ability of the β-carboxyl-substituted ChlFe to selectively reproduce this biological hydroxylation pathway, which is in contrast to the varying pathways observed with other ligand architectures, demonstrates that it is an

https://doi.org/10.1021/acs.est.5c10288
Environ. Sci. Technol. 2026, 60, 2728−2741

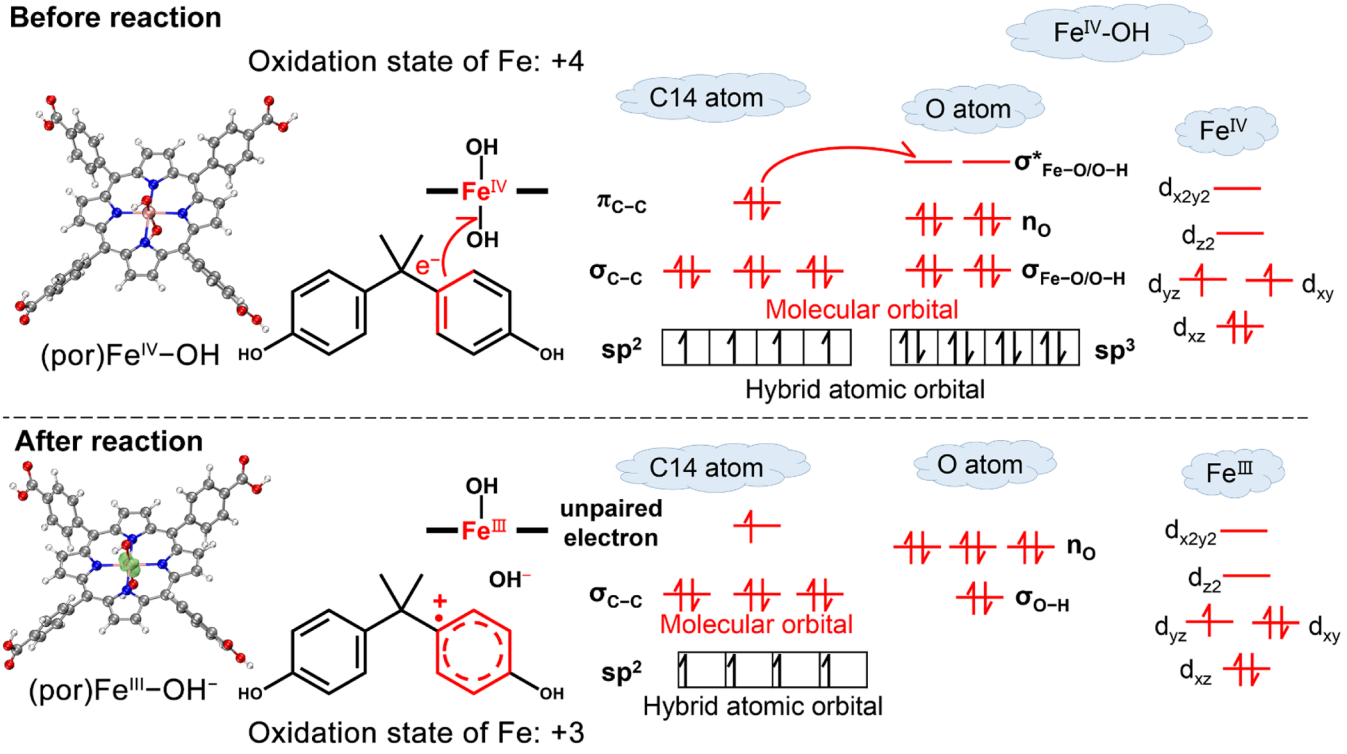

Figure 6. Distribution of the spin density and SET reaction mechanism for BPA degradation by (por)Fe^{IV}–OH at C14. Electron donation from the π-conjugated system of BPA to the σ^*_{Fe-O} orbital cleaves the Fe–O bond, yielding TCPFe and a transient BPA radical cation (BPA$\bullet^+$).

effective biomimetic model and confirms that ligand coordination is a primary driver for pathway selectivity.

The initiation of the OAF reaction is triggered by hydrogen abstraction from the C12 position of BPA, which is facilitated by the radical character inherent in the porphyrin ring. The C12 atom within BPA exhibits sp^2 hybridization, characterized by three $\sigma_{C-C/C-H}$ orbitals and one π_{C-C} orbital, along with their corresponding antibonding orbitals ($\sigma^*_{C-C/C-H}$ and π^*_{C-C}). The unpaired electron from the chlorin ring transfers to the π^*_{Fe-O} orbital of the O atom, disrupting the π_{Fe-O} orbital and reducing the chlorin ring cation radical ((Chl)$^{\bullet+}$) to Chl. Subsequently, the resulting unpaired electrons on O further transfers to σ^*_{C-H} of the C12, breaking σ_{C-H} orbital and forming a σ_{O-H} orbital (Figure 5). Significantly, the iron center remains in the +4 oxidation state (Figure S8), thereby retaining its high oxidizing power for further attack. Consequently, the unpaired electron on C12 is transferred to the σ^*_{Fe-O} orbital, breaking the σ_{Fe-O} orbital and forming a new σ_{C-O} orbital. As a result, BPA is transformed into the hydroxylation products (DP-243), and (Chl)$^{\bullet+}$Fe^{IV}=O is reduced into ChlFe. Furthermore, DP-243 can undergo additional hydroxylation via the OAF pathway with (Chl)$^{\bullet+}$Fe^{IV}=O to yield DP-259 and DP-291. Subsequent reactions involving these hydroxylation products and (Chl)$^{\bullet+}$Fe^{IV}=O lead to the formation of products, including DP-197, DP-181, DP-151, and DP-109 (as illustrated in Figure 3a).

3.5. Ring-Cleavage via SET Pathway in the TCPFe/H_2O_2 System

The degradation of BPA in the TCPFe/H_2O_2 system primarily proceeds via electrophilic attack, as the generated active species (por)Fe^{IV}–OH exhibits electron affinity. SET reaction mediated by (por)Fe^{IV}–OH is thermodynamically favorable (Figure 4b). The SET pathway involves the transfer of an electron from BPA to (por)Fe^{IV}–OH. HOMO and f^- results indicate that C14 is the most active site for electrophilic attack (Figure 3b,c). The C14 atom of BPA exhibits sp^2 hybridization, including three σ_{C-C} orbitals and one π_{C-C} orbital. Based on the comparative analysis of bond orders before and after an electron loss in BPA (Text S5), (por)Fe^{IV}–OH captures an electron from the conjugate π-system of BPA via the C14 site. The molecular orbital interactions between BPA and (por)Fe^{IV}–OH were illustrated based on the changes in oxidation state and spin density analysis (Figure 6). Consistent with the electronic structure of the Fe^{IV}–OH species in P450 characterized by Shaik et al.,[16,69] the Fe^{IV} center is analyzed in its triplet spin state, characterized by two unpaired electrons in the Fe(3d) orbitals. An electron from the π-system of BPA was transferred to σ^*_{Fe-O} of (por)Fe^{IV}–OH via the C14 site, facilitating cleavage of the σ_{Fe-O}, reduction of (por)Fe^{IV}–OH to TCPFe, and formation of OH$^-$ and a BPA radical cation (BPA$\bullet^+$). This destabilization of BPA$\bullet^+$ renders the ring highly susceptible to subsequent attack of the coexisting HO$^\bullet$ with high redox potential, leading to the cleavage of the aromatic ring and formation of the unique ring-opened products (e.g., DP-165, DP-87, DP-73, and DP-57) observed exclusively in the TCPFe/H_2O_2 system (Figure 3a). In addition, BPA was also attacked by HO$^\bullet$ via the HAA pathway to generate products such as DP-243 and DP-241 (Text S6).

3.6. Quinonization via a Coupled SET-HAA Pathway in the TSPFe/H_2O_2 System

BPA exhibits characteristic quinonization degradation products in the TSPFe/H_2O_2 system, where the generated active species of [(por)Fe^{IV}–OH]$^+$ and $HO_2^\bullet$ mediate BPA degradation through the SET and HAA pathways. The degradation of BPA by [(por)Fe^{IV}–OH]$^+$ via the SET pathway is supported by

https://doi.org/10.1021/acs.est.5c10288
Environ. Sci. Technol. 2026, 60, 2728–2741

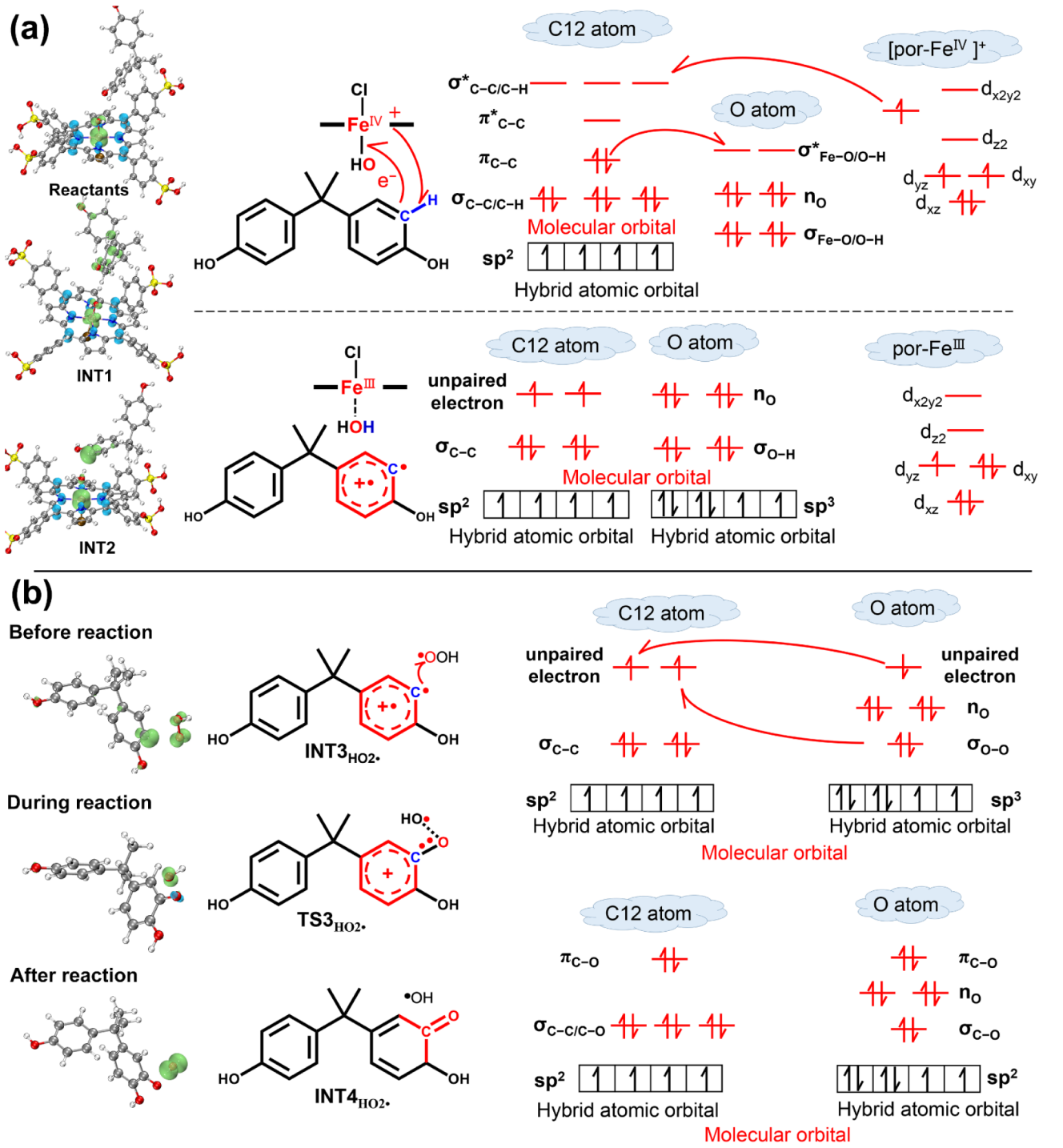

Figure 7. Spin density evolution and the coupled SET-HAA mechanism for BPA degradation by [(por)Fe^{IV}−OH]$^+$ and $HO_2^•$. (a) The coupled SET-HAA process, where electron transfer from BPA to [(por)Fe^{IV}−OH]$^+$ triggers Fe−O bond cleavage, and then the H atom at C12 was abstracted to form TSPFe, H_2O, and the intermediate [BPA(−H)•]$^{•+}$. (b) The subsequent reaction between [BPA(−H)•]$^{•+}$ and $HO_2^•$, where unpaired electrons on C12 and O atoms were paired to induce O−O bond cleavage and C−O bond formation, leading to quinone-type products.

kinetic analysis (Figure 4b). The direct HAA barrier for [(por)Fe^{IV}−OH]$^+$ is relatively high (23.6 kcal/mol), which is consistent with the consensus that Compound II is a sluggish oxidant for H-abstraction compared to Compound I.[69,70] The bond elongation to 1.923 Å during reaction indicates reduction to Fe(III) by the SET pathway (Table S4), and the coupled SET-HAA degradation pathway has been further validated through analysis of spin density distribution and oxidation state. As spin density gradually distributes onto the BPA molecule (Figure 7a), the oxidation state of BPA increases from 0 to 1, while the oxidation state of Fe decreases from +4 to +3 (Figure S9), indicating a single-electron transfer from BPA to [(por)Fe^{IV}−OH]$^+$. As the reaction proceeds, the hydrogen atom bonded to C12 gradually forms a bond with the O atom of [(por)Fe^{IV}−OH]$^+$. Therefore, the [(por)Fe^{IV}−OH]$^+$-driven coupled SET-HAA pathway proceeds with three key steps: (i) electron transfer from the conjugated π-system of BPA to [(por)Fe^{IV}−OH]$^+$, (ii) cleavage of the C12−H bonds,

https://doi.org/10.1021/acs.est.5c10288
Environ. Sci. Technol. 2026, 60, 2728−2741

(a)

Feature	ChlFe/H_2O_2 system	TCPFe/H_2O_2 system	TSPFe/H_2O_2 system
Ligand substitution	β-carboxyl	meso-carboxyl	meso-sulfoxyl
Observed kinetics	Pseudo-second-order	Pseudo-first-order	Pseudo-first-order
Rate constant (k_{obs})	69.3 $L \cdot mmol^{-1} \cdot min^{-1}$	0.4 min^{-1}	0.6 min^{-1}
Active species	$(Chl)^{\bullet+}Fe^{IV}=O$	$(por)Fe^{IV}-OH$ and $HO^{\bullet}$	$[(por)Fe^{IV}-OH]^{+}$ and $HO_2^{\bullet}$
Dominant pathway	Hydroxylation	Ring-cleavage	Quinonization
Key mechanism	OAF	SET-initiated radical attack	Coupled SET-HAA
Matrix resistance	High	Low	Low

(b)

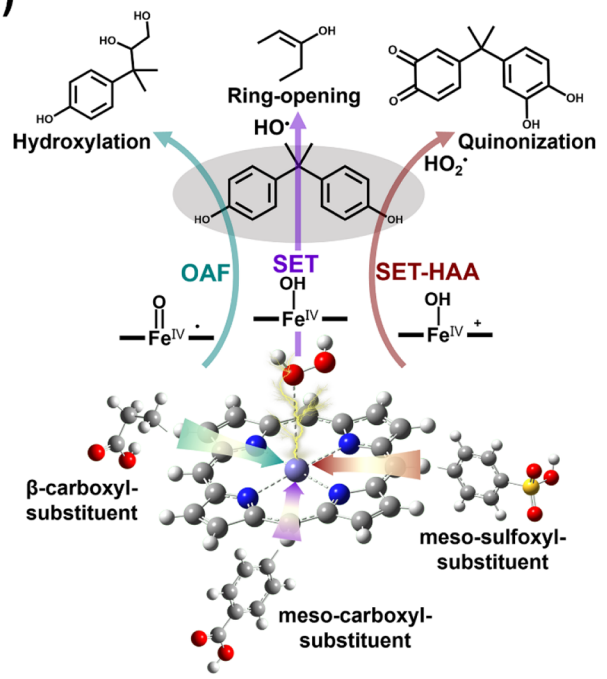

Figure 8. (a) Comparative summary of coordination-dependent catalytic systems. The *β*-substituted ChlFe produces $(Chl)^{\bullet+}Fe^{IV}=O$, while meso-substituted TCPFe and TSPFe generate $(por)Fe^{IV}-OH$ and $[(por)Fe^{IV}-OH]^{+}$ accompanied by $HO^{\bullet}$ and $HO_2^{\bullet}$, respectively. (b) Mechanistic illustration of the corresponding degradation pathways of BPA affected by the coordination effect of iron-based catalysts. OAF-mediated hydroxylation by $(Chl)^{\bullet+}Fe^{IV}=O$, SET-induced ring cleavage by $(por)Fe^{IV}-OH/HO^{\bullet}$, and coupled SET−HAA-driven quinonization by $[(por)Fe^{IV}-OH]^{+}/HO_2^{\bullet}$.

and (iii) formation of the O−H bond. Similar to the neutral species, the Fe^{IV} in cationic $[(por)Fe^{IV}-OH]^{+}$ also adopts a triplet spin state in accordance with theoretical benchmarks.[71,72] During the reaction, an electron is transferred from the conjugated *π*-system of BPA into σ^*_{Fe-O}, promoting the cleavage of the Fe−O bond and reducing Fe^{IV} to Fe^{III}. Subsequently, the unpaired electron of $[(por)Fe^{IV}-OH]^{+}$ is transferred to the σ^*_{C-H} orbital, facilitating cleavage of the C−H bond to generate TSPFe, H_2O molecule and $[BPA(-H)\bullet]^{\bullet+}$ (Figure 7a). This highly reactive $[BPA(-H)\bullet]^{\bullet+}$ intermediate can be further attacked by coexisting $HO_2^{\bullet}$ radicals in the TSPFe/H_2O_2 system, which have a high affinity for the radical cation. $[BPA(-H)\bullet]^{\bullet+}$ contains two unpaired electrons, mainly localized on the C12 atom. The O atom of $HO_2^{\bullet}$ exhibits sp^3 hybridization, comprising one σ_{O-O} orbital, two nonbonding orbitals (n_0), and one orbital occupied by an unpaired electron. Mechanistically, the unpaired electron on the O atom of $HO_2^{\bullet}$ pairs with the unpaired electron on the C12 atom of $[BPA(-H)\bullet]^{\bullet+}$ to form a σ_{C-O} orbital. Meanwhile, the second unpaired electron on C12 triggers the homolytic cleavage of the O−O bond in $HO_2^{\bullet}$. This electron then pairs with the newly formed unpaired electron on the O orbital to form a π_{C-O} orbital (Figure 7b), ultimately driving the formation of the quinone product in the TSPFe/H_2O_2 system (Figure 3a). Additionally, $HO_2^{\bullet}$ can directly initiate HAA at the phenolic hydroxyl group (O17 site) of BPA, which also leads to quinonization products such as DP-259 (Text S7).

4. ENVIRONMENTAL IMPLICATIONS

This study elucidates that the reactivity of high-valent iron-oxo species in environmental remediation is not intrinsic but is intimately governed by the catalyst's coordination environment. By systematically comparing *β*- and *meso*-substituted iron porphyrins, we demonstrated that ligand positioning dictates the nature of active species and the subsequent degradation pathways (Figure 8a,b). This coordination-dependent selectivity is rationalized by the electric-field effect,[64] where *meso*-charged substituents stabilize electron-acceptor orbitals to favor SET-initiated pathways, while *β*-substituents support direct oxygen transfer. The discovery indicates that rational ligand engineering can predictably steer pollutant transformation at the molecular level. Crucially, we found that the $Fe^{IV}=O$-mediated OAF pathway exhibits superior tolerance to complex matrices compared to $Fe^{IV}-OH$/radical-based SET pathways. A key implication for creating robust and efficient systems in complex environmental matrices is that catalytic designs should favor direct oxygen-atom transfer from an active species, rather than pathways that release small, nonselective free radicals into the bulk solution. These findings establish a foundational mechanistic principle that may inform the rational design of next-generation biomimetic catalysts, enabling the more targeted and efficient transformation of organic pollutants within complex environmental matrices.

■ ASSOCIATED CONTENT

Supporting Information

The Supporting Information is available free of charge at https://pubs.acs.org/doi/10.1021/acs.est.5c10288.

Chemicals (Text S1); computational and analytical methods and details (Text S2); additional discussion of SET and HAA pathways (Texts S3, S5−S7); discussion of the ChlFe/H_2O_2 system (Text S4);

https://doi.org/10.1021/acs.est.5c10288
Environ. Sci. Technol. 2026, 60, 2728−2741

degradation product identification (Table S1); Fukui index of C and H atoms in the BPA molecule (Tables S2 and S3); comparative summary of reaction parameters for high-valent iron-oxo species (Table S4); kinetic parameters of the SET pathway (Table S5); bond order of intermediates (Tables S6−S7); molecular structures of three catalysts, supplementary kinetics, PMSO probe results, mass analysis, toxicity analysis, and DFT computational data (Figures S1−S12) (PDF)

AUTHOR INFORMATION

Corresponding Authors

Jingping Hu − *Hubei Key Laboratory of Multi-Media Pollution Cooperative Control in Yangtze Basin, School of Environmental Science and Engineering, Huazhong University of Science and Technology (HUST), Wuhan, Hubei 430074, P. R. China; Hubei Provincial Engineering Laboratory of Solid Waste Treatment, Disposal and Recycling, Wuhan, Hubei 430074, China;* orcid.org/0000-0001-9984-6636; Email: hujp@hust.edu.cn

Huijie Hou − *Hubei Key Laboratory of Multi-Media Pollution Cooperative Control in Yangtze Basin, School of Environmental Science and Engineering, Huazhong University of Science and Technology (HUST), Wuhan, Hubei 430074, P. R. China; Hubei Provincial Engineering Laboratory of Solid Waste Treatment, Disposal and Recycling, Wuhan, Hubei 430074, China;* orcid.org/0000-0002-6968-8080; Email: houhuijie@hust.edu.cn

Authors

Xiaorong Yang − *Guangdong-Hong Kong-Macao Joint Laboratory for Contaminants Exposure and Health, Guangdong Key Laboratory of Environmental Catalysis and Health Risk Control, Institute of Environmental Health and Pollution Control, Guangdong University of Technology, Guangzhou 510006, P. R. China; Hubei Key Laboratory of Multi-Media Pollution Cooperative Control in Yangtze Basin, School of Environmental Science and Engineering, Huazhong University of Science and Technology (HUST), Wuhan, Hubei 430074, P. R. China; Hubei Provincial Engineering Laboratory of Solid Waste Treatment, Disposal and Recycling, Wuhan, Hubei 430074, China; Guangdong Basic Research Center of Excellence for Ecological Security and Green Development, Key Laboratory of City Cluster Environmental Safety and Green Development of the Ministry of Education, School of Environmental Science and Engineering, Guangdong University of Technology, Guangzhou 510006, China*

Qiongbin Zheng − *Guangdong-Hong Kong-Macao Joint Laboratory for Contaminants Exposure and Health, Guangdong Key Laboratory of Environmental Catalysis and Health Risk Control, Institute of Environmental Health and Pollution Control, Guangdong University of Technology, Guangzhou 510006, P. R. China*

Longsheng Wu − *Hubei Key Laboratory of Multi-Media Pollution Cooperative Control in Yangtze Basin, School of Environmental Science and Engineering, Huazhong University of Science and Technology (HUST), Wuhan, Hubei 430074, P. R. China; Hubei Provincial Engineering Laboratory of Solid Waste Treatment, Disposal and Recycling, Wuhan, Hubei 430074, China*

Guiying Li − *Guangdong-Hong Kong-Macao Joint Laboratory for Contaminants Exposure and Health, Guangdong Key Laboratory of Environmental Catalysis and Health Risk Control, Institute of Environmental Health and Pollution Control, Guangdong University of Technology, Guangzhou 510006, P. R. China; Guangdong Basic Research Center of Excellence for Ecological Security and Green Development, Key Laboratory of City Cluster Environmental Safety and Green Development of the Ministry of Education, School of Environmental Science and Engineering, Guangdong University of Technology, Guangzhou 510006, China*

Taicheng An − *Guangdong-Hong Kong-Macao Joint Laboratory for Contaminants Exposure and Health, Guangdong Key Laboratory of Environmental Catalysis and Health Risk Control, Institute of Environmental Health and Pollution Control, Guangdong University of Technology, Guangzhou 510006, P. R. China; Guangdong Basic Research Center of Excellence for Ecological Security and Green Development, Key Laboratory of City Cluster Environmental Safety and Green Development of the Ministry of Education, School of Environmental Science and Engineering, Guangdong University of Technology, Guangzhou 510006, China*

Jiakuan Yang − *Hubei Key Laboratory of Multi-Media Pollution Cooperative Control in Yangtze Basin, School of Environmental Science and Engineering, Huazhong University of Science and Technology (HUST), Wuhan, Hubei 430074, P. R. China; Hubei Provincial Engineering Laboratory of Solid Waste Treatment, Disposal and Recycling, Wuhan, Hubei 430074, China*

Complete contact information is available at: https://pubs.acs.org/10.1021/acs.est.5c10288

Notes

The authors declare no competing financial interest.

ACKNOWLEDGMENTS

This work was supported by the National Natural Science Foundation of China (52170134, 52222006, and 52070083), the National Key Research and Development Program of China (2023YFC3902802), the Interdisciplinary Research Program of Huazhong University of Science and Technology (HUST, 2023JCYJ005), Wuhan Power Battery Low-carbon Recycling Industry Innovation Joint Laboratory (2025020802040290), and the Hubei Provincial Science and Technology Research Project (2024BAA012, 2025CSA138). The authors acknowledge the Public Service Platform of Environmental Research Facilities at the School of Environmental Science and Engineering, HUST, the Analytical and Testing Center of HUST, and the Analysis and Test Center of Guangdong University of Technology for providing characterization facilities, and the public computing service platform provided by the HPC platform at the Network and Computing Center of HUST to support the computing work.

REFERENCES

(1) Zhou, H.; Zhong, S.; Chen, J.; Ren, S.; Ren, W.; Lai, B.; Guan, X.; Ma, T.; Wang, S.; Duan, X. Overlooked complexation and competition effects of phenolic contaminants in a Mn(II)/nitrilotriacetic acid/peroxymonosulfate system: inhibited generation of primary and secondary high-valent manganese species. *Environ. Sci. Technol.* **2024**, *58* (42), 19080−19089.

(2) Zhu, L.; Ji, J.; Liu, J.; Mine, S.; Matsuoka, M.; Zhang, J.; Xing, M. Designing 3D-MoS_2 sponge as excellent cocatalysts in advanced oxidation processes for pollutant control. *Angew. Chem., Int. Ed.* **2020**, *59* (33), 13968−13976.
(3) Wang, J.; Wang, S. Activation of persulfate (PS) and peroxymonosulfate (PMS) and application for the degradation of emerging contaminants. *Chem. Eng. J.* **2018**, *334*, 1502−1517.
(4) Xie, Z. H.; He, C. S.; Zhou, H. Y.; Li, L. L.; Liu, Y.; Du, Y.; Liu, W.; Mu, Y.; Lai, B. Effects of molecular structure on organic contaminants' degradation efficiency and dominant ROS in the advanced oxidation process with multiple ROS. *Environ. Sci. Technol.* **2022**, *56* (12), 8784−8795.
(5) Wei, Y.; Song, P.; Wen, Y.; Liao, Q.; Du, X.; Chen, L.; Liang, J.; Long, G.; Shimaoka, T. In-depth analysis of the roles and mechanisms of sulfate radical and hydroxyl radical in the degradation of metal-cyanide complexes. *Water Res.* **2025**, *268*, 122656.
(6) Liu, X.; Liu, Y.; Qin, H.; Ye, Z.; Wei, X.; Miao, W.; Yang, D.; Mao, S. Selective removal of phenolic compounds by peroxydisulfate activation: Inherent role of hydrophobicity and interface ROS. *Environ. Sci. Technol.* **2022**, *56* (4), 2665−2676.
(7) Liu, T.; Xiao, S.; Li, N.; Chen, J.; Zhou, X.; Qian, Y.; Huang, C.; Zhang, Y. Water decontamination via nonradical process by nanoconfined Fenton-like catalysts. *Nat. Commun.* **2023**, *14* (1), 2881.
(8) Zhang, T.; Yang, P.; Ji, Y.; Lu, J. The role of natural organic matter in the degradation of phenolic pollutants by sulfate radical oxidation: radical scavenging vs reduction. *Environ. Sci. Technol.* **2025**, *59* (6), 3325−3335.
(9) Lau, S. S.; Abraham, S. M.; Roberts, A. L. Chlorination revisited: does Cl^- serve as a catalyst in the chlorination of phenols? *Environ. Sci. Technol.* **2016**, *50* (24), 13291−13298.
(10) Li, Y.; Hu, J.; Bao, Y.; Xiao, Y.; Lin, L.; Li, B.; Li, X. High-valent iron−oxo species in heterogeneous catalysis: Formation, mechanism, and reactivity for the degradation of various emerging organic contaminants. *Chem. Eng. J.* **2024**, *501*, 157490.
(11) Zhou, Z.; Li, M.; Kuai, C.; Zhang, Y.; Smith, V. F.; Lin, F.; Aiello, A.; Durkin, D. P.; Chen, H.; Shuai, D. Fe-based single-atom catalysis for oxidizing contaminants of emerging concern by activating peroxides. *J. Hazard. Mater.* **2021**, *418*, 126294.
(12) Kohantorabi, M.; Moussavi, G.; Giannakis, S. A review of the innovations in metal- and carbon-based catalysts explored for heterogeneous peroxymonosulfate (PMS) activation, with focus on radical vs. non-radical degradation pathways of organic contaminants. *Chem. Eng. J.* **2021**, *411*, 127957.
(13) Pestovsky, O.; Bakac, A. Reactivity of aqueous Fe(IV) in hydride and hydrogen atom transfer reactions. *J. Am. Chem. Soc.* **2004**, *126* (42), 13757−13764.
(14) Wang, Z.; Qiu, W.; Pang, S.; Guo, Q.; Guan, C.; Jiang, J. Aqueous iron(IV)−oxo complex: An emerging powerful reactive oxidant formed by iron(II)-based advanced oxidation processes for oxidative water treatment. *Environ. Sci. Technol.* **2022**, *56* (3), 1492−1509.
(15) Shaik, S.; Kumar, D.; de Visser, S. P.; Altun, A.; Thiel, W. Theoretical perspective on the structure and mechanism of cytochrome P450 enzymes. *Chem. Rev.* **2005**, *105* (6), 2279−2328.
(16) Meunier, B.; de Visser, S. P.; Shaik, S. Mechanism of oxidation reactions catalyzed by cytochrome P450 enzymes. *Chem. Rev.* **2004**, *104* (9), 3947−3980.
(17) Shaik, S.; Chen, H.; Usharani, D.; Thiel, W. QM/MM studies of structure and reactivity of cytochrome P450 enzymes: methodology and selected applications. *Drug Metabolism Prediction.* **2014**, *311*, 133−178.
(18) Shaik, S.; De Visser, S. P. Computational approaches to cytochrome P450 function. In *Cytochrome P450: structure, mechanism, and biochemistry*, Ortiz de Montellano, P. R., Eds.; Springer US: Boston, MA, 2005; pp. 45−85.
(19) Stone, K. L.; Hoffart, L. M.; Behan, R. K.; Krebs, C.; Green, M. T. Evidence for two ferryl species in chloroperoxidase compound II. *J. Am. Chem. Soc.* **2006**, *128* (18), 6147−6153.
(20) de Visser, S. P.; Kumar, D.; Cohen, S.; Shacham, R.; Shaik, S. A predictive pattern of computed barriers for C−H hydroxylation by compound I of cytochrome P450. *J. Am. Chem. Soc.* **2004**, *126* (27), 8362−8363.
(21) Ogliaro, F.; Harris, N.; Cohen, S.; Filatov, M.; de Visser, S. P.; Shaik, S. A model "rebound" mechanism of hydroxylation by cytochrome P450: stepwise and effectively concerted pathways, and their reactivity patterns. *J. Am. Chem. Soc.* **2000**, *122* (37), 8977−8989.
(22) Sorokin, A. B. Phthalocyanine metal complexes in catalysis. *Chem. Rev.* **2013**, *113* (10), 8152−8191.
(23) İşci, Ü.; Faponle, A. S.; Afanasiev, P.; Albrieux, F.; Briois, V.; Ahsen, V.; Dumoulin, F.; Sorokin, A. B.; de Visser, S. P. Site-selective formation of an iron(iv)−oxo species at the more electron-rich iron atom of heteroleptic μ-nitrido diiron phthalocyanines. *Chem. Sci.* **2015**, *6* (8), 5063−5075.
(24) Quesne, M. G.; Senthilnathan, D.; Singh, D.; Kumar, D.; Maldivi, P.; Sorokin, A. B.; de Visser, S. P. Origin of the enhanced reactivity of μ-nitrido-bridged diiron(IV)-oxo porphyrinoid complexes over cytochrome P450 compound I. *ACS Catal.* **2016**, *6* (4), 2230−2243.
(25) Shaik, S.; Stuyver, T. Introduction to the Book. In *Effects of Electric Fields on Structure and Reactivity: new Horizons in Chemistry*, Shaik, S.; Stuyver, T.; The Royal Society of Chemistry, 2021.
(26) Shaik, S.; Danovich, D.; Joy, J.; Wang, Z.; Stuyver, T. Electric-field mediated chemistry: uncovering and exploiting the potential of (oriented) electric fields to exert chemical catalysis and reaction control. *J. Am. Chem. Soc.* **2020**, *142* (29), 12551−12562.
(27) Shaik, S.; Mandal, D.; Ramanan, R. Oriented electric fields as future smart reagents in chemistry. *Nat. Chem.* **2016**, *8* (12), 1091−1098.
(28) Shaik, S.; Ramanan, R.; Danovich, D.; Mandal, D. Structure and reactivity/selectivity control by oriented-external electric fields. *Chem. Soc. Rev.* **2018**, *47* (14), 5125−5145.
(29) Shaik, S.; de Visser, S. P.; Kumar, D. External electric field will control the selectivity of enzymatic-like bond activations. *J. Am. Chem. Soc.* **2004**, *126* (37), 11746−11749.
(30) Stuyver, T.; Danovich, D.; Joy, J.; Shaik, S. External electric field effects on chemical structure and reactivity. *WIREs Comput. Mol. Sci.* **2020**, *10* (2), No. e1438.
(31) Lin, Y.; Wang, Y.; Weng, Z.; Zhou, Y.; Liu, S.; Ou, X.; Xu, X.; Cai, Y.; Jiang, J.; Han, B.; et al. Coordination engineering of heterogeneous high-valent Fe(IV)-oxo for safe removal of pollutants via powerful Fenton-like reactions. *Nat. Commun.* **2024**, *15* (1), 10032.
(32) Chen, T.; Zhang, G.; Sun, H.; Hua, Y.; Yang, S.; Zhou, D.; Di, H.; Xiong, Y.; Hou, S.; Xu, H.; et al. Robust Fe-N_4-C_6O_2 single atom sites for efficient PMS activation and enhanced Fe^{IV} = O reactivity. *Nat. Commun.* **2025**, *16* (1), 2402.
(33) Zeng, T.; Tang, X.; Huang, Z.; Chen, H.; Jin, S.; Dong, F.; He, J.; Song, S.; Zhang, H. Atomically dispersed Fe−N_4 site as a conductive bridge enables efficient and stable activation of peroxymonosulfate: active site renewal, anti-oxidative capacity, and pathway alternation mechanism. *Environ. Sci. Technol.* **2023**, *57* (49), 20929−20940.
(34) Huang, B.; Wu, Z.; Wang, X.; Song, X.; Zhou, H.; Zhang, H.; Zhou, P.; Liu, W.; Xiong, Z.; Lai, B. Coupled surface-confinement effect and pore engineering in a single-Fe-atom catalyst for ultrafast Fenton-like reaction with high-valent iron-oxo complex oxidation. *Environ. Sci. Technol.* **2023**, *57* (41), 15667−15679.
(35) Zhang, B.; Li, X.; Akiyama, K.; Bingham, P. A.; Kubuki, S. Elucidating the mechanistic origin of a spin state-dependent FeNx−C catalyst toward organic contaminant oxidation via peroxymonosulfate activation. *Environ. Sci. Technol.* **2022**, *56* (2), 1321−1330.
(36) Qian, K.; Chen, H.; Li, W.; Ao, Z.; Wu, Y.-N.; Guan, X. Single-atom Fe catalyst outperforms its homogeneous counterpart for activating peroxymonosulfate to achieve effective degradation of organic contaminants. *Environ. Sci. Technol.* **2021**, *55* (10), 7034−7043.

https://doi.org/10.1021/acs.est.5c10288
Environ. Sci. Technol. 2026, 60, 2728−2741

(37) Traylor, T. G.; Tsuchiya, S.; Byun, Y. S.; Kim, C. High-yield epoxidations with hydrogen peroxide and tert-butyl hydroperoxide catalyzed by iron(III) porphyrins: heterolytic cleavage of hydroperoxides. *J. Am. Chem. Soc.* **1993**, *115* (7), 2775−2781.
(38) Groves, J. T.; Nemo, T. E. Aliphatic hydroxylation catalyzed by iron porphyrin complexes. *J. Am. Chem. Soc.* **1983**, *105* (20), 6243−6248.
(39) Sharma, V. K.; Feng, M.; Dionysiou, D. D.; Zhou, H.-C.; Jinadatha, C.; Manoli, K.; Smith, M. F.; Luque, R.; Ma, X.; Huang, C.-H. Reactive high-valent iron intermediates in enhancing treatment of water by ferrate. *Environ. Sci. Technol.* **2022**, *56* (1), 30−47.
(40) Xie, J.; Wu, S.; Luo, C.; Zou, J.; Lin, Y.; He, S.; Yang, C. Modulating electronic structure of active sites on iron-based nanoparticles enhances peroxymonosulfate activation. *Appl. Catal., B* **2024**, *354*, 124138.
(41) Gao, X.; Li, J.; Chen, J.; Che, H.; Wang, P.; Liu, B.; Ao, Y. New insight into the mechanism of symmetry-breaking charge separation induced high-valent iron(IV) for highly efficient photodegradation of organic pollutants. *Appl. Catal., B* **2023**, *321*, 122066.
(42) Niwa, T.; Fujimoto, M.; Kishimoto, K.; Yabusaki, Y.; Ishibashi, F.; Katagiri, M. Metabolism and interaction of bisphenol A in human hepatic cytochrome P450 and steroidogenic CYP17. *Biol. Pharm. Bull.* **2001**, *24* (9), 1064−1067.
(43) Sasaki, M.; Akahira, A.; Oshiman, K.-I.; Tsuchido, T.; Matsumura, Y. Purification of cytochrome P450 and ferredoxin, involved in bisphenol A degradation, from *Sphingomonas sp.* strain AO1. *Appl. Environ. Microbiol.* **2005**, *71* (12), 8024−8030.
(44) Wang, W.; Yu, H.; Qin, H.; Long, Y.; Ye, J.; Qu, Y. Bisphenol A degradation pathway and associated metabolic networks in Escherichia coli harboring the gene encoding CYP450. *J. Hazard. Mater.* **2020**, *388*, 121737.
(45) Zhang, X.; Wasson, M. C.; Shayan, M.; Berdichevsky, E. K.; Ricardo-Noordberg, J.; Singh, Z.; Papazyan, E. K.; Castro, A. J.; Marino, P.; Ajoyan, Z.; Chen, Z.; Islamoglu, T.; Howarth, A. J.; Liu, Y.; Majewski, M. B.; Katz, M. J.; Mondloch, J. E.; Farha, O. K. A historical perspective on porphyrin-based metal−organic frameworks and their applications. *Coord. Chem. Rev.* **2021**, *429*, 213615.
(46) Hermano Sampaio Dias, A.; Yadav, R.; Mokkawes, T.; Kumar, A.; Skaf, M. S.; Sastri, C. V.; Kumar, D.; de Visser, S. P. Biotransformation of bisphenol by human cytochrome P450 2C9 enzymes: A density functional theory study. *Inorg. Chem.* **2023**, *62* (5), 2244−2256.
(47) Yang, X.; Hu, J.; Wu, L.; Hou, H.; Liang, S.; Yang, J. Cooperation of multiple active species generated in hydrogen peroxide activation by iron porphyrin for phenolic pollutants degradation. *Environ. Pollut.* **2022**, *313*, 120097.
(48) Yang, X.; Zhang, P.; Hou, H.; Hu, J.; Liu, L.; Wu, L.; Chen, S.; Pan, K.; Liang, S.; Yuan, S.; Yang, J. An iron chlorophyll derivative for enhanced degradation of bisphenol A: New insight into the generation mechanism of high-valent iron oxo species. *Chem. Eng. J.* **2023**, *451*, 138688.
(49) Zhang, H.; Xie, C.; Chen, L.; Duan, J.; Li, F.; Liu, W. Different reaction mechanisms of $SO_4^{\bullet-}$ and •OH with organic compound interpreted at molecular orbital level in Co(II)/peroxymonosulfate catalytic activation system. *Water Res.* **2023**, *229*, 119392.
(50) Thomas, J.; Mokkawes, T.; Senft, L.; Dey, A.; Gordon, J. B.; Ivanovic-Burmazovic, I.; de Visser, S. P.; Goldberg, D. P. Axial ligation impedes proton-coupled electron-transfer reactivity of a synthetic compound-I analogue. *J. Am. Chem. Soc.* **2024**, *146* (18), 12338−12354.
(51) Bielski, B. H. J.; Cabelli, D. E.; Arudi, R. L.; Ross, A. B. Reactivity of HO_2/O_2^- radicals in aqueous solution. *J. Phys. Chem. Ref. Data* **1985**, *14* (4), 1041−1100.
(52) Buxton, G. V.; Greenstock, C. L.; Helman, W. P.; Ross, A. B. Critical review of rate constants for reactions of hydrated electrons, hydrogen atoms and hydroxyl radicals (•OH/•O$^-$) in aqueous solution. *J. Phys. Chem. Ref. Data* **1988**, *17* (2), 513−886.
(53) Jiang, Q.; Ma, Y.; Zhao, P.; Li, X.; Shao, Y.; Xu, X. Electronic structure regulation of Fe sites by coordinating moieties in the Fenton-like process enables tunable water decontamination. *Environ. Sci. Technol.* **2025**, *59* (27), 14182−14192.
(54) Li, J.; Yang, L.; Cui, Y.; Yang, Z.; Zeng, G.; Pan, B. Peroxide directing the iron cycling for tailored generation of active oxidants in aqueous Fenton reactions. *Environ. Sci. Technol.* **2025**, *59* (6), 3316−3324.
(55) Fujii, H. Effects of the electron-withdrawing power of substituents on the electronic structure and reactivity in oxoiron(IV) porphyrin.pi.-cation radical complexes. *J. Am. Chem. Soc.* **1993**, *115* (11), 4641−4648.
(56) Nakagawa, Y.; Suzuki, T. Metabolism of bisphenol A in isolated rat hepatocytes and oestrogenic activity of a hydroxylated metabolite in MCF-7 human breast cancer cells. *Xenobiotica* **2001**, *31* (3), 113−123.
(57) Morohoshi, K.; Shiraishi, F.; Oshima, Y.; Koda, T.; Nakajima, N.; Edmonds, J. S.; Morita, M. Synthesis and estrogenic activity of bisphenol A mono- and di-β-D-glucopyranosides, plant metabolites of bisphenol A. *Environ. Toxicol. Chem.* **2003**, *22* (10), 2275−2279.
(58) Chen, Y.; Shao, Y.; Li, O.; Liang, J.; Tang, S.; Li, Z. WS2-cocatalyzed peroxymonosulfate activation via an enhanced Fe(III)/Fe(II) cycle toward efficient organic pollutant degradation. *Chem. Eng. J.* **2022**, *442*, 135961.
(59) Cheng, K.; Cai, Z.; Fu, J.; Sun, X.; Sun, W.; Chen, L.; Zhang, D.; Liu, W. Synergistic adsorption of Cu(II) and photocatalytic degradation of phenanthrene by a jaboticaba-like TiO2/titanate nanotube composite: An experimental and theoretical study. *Chem. Eng. J.* **2019**, *358*, 1155−1165.
(60) Chen, Z.; Yin, G. The reactivity of the active metal oxo and hydroxo intermediates and their implications in oxidations. *Chem. Soc. Rev.* **2015**, *44* (5), 1083−1100.
(61) Armstrong, D. A.; Huie, R. E.; Koppenol, W. H.; Lymar, S. V.; Merényi, G.; Neta, P.; Ruscic, B.; Stanbury, D. M.; Steenken, S.; Wardman, P. Standard electrode potentials involving radicals in aqueous solution: inorganic radicals. *Pure Appl. Chem.* **2015**, *87* (11−12), 1139−1150.
(62) Green, M. T.; Dawson, J. H.; Gray, H. B. Oxoiron(IV) in chloroperoxidase compound II is basic: implications for P450 chemistry. *Science* **2004**, *304* (5677), 1653−1656.
(63) Huang, X.; Groves, J. T. Oxygen activation and radical transformations in heme proteins and metalloporphyrins. *Chem. Rev* **2018**, *118* (5), 2491−2553.
(64) Yadav, S.; Shaik, S.; Siddiqui, S. A.; Kalita, S.; Dubey, K. D. Local electric fields dictate function: the different product selectivities observed for fatty acid oxidation by two deceptively very similar P450-peroxygenases OleT and BSβ. *J. Chem. Inf. Model.* **2022**, *62* (4), 1025−1035.
(65) Lu, T. *TSTcalculator*, 2020. http://sobereva.com/310.
(66) Kumar, D.; Sastry, G. N.; de Visser, S. P. Axial ligand effect on the rate constant of aromatic hydroxylation by iron(IV)−oxo complexes mimicking cytochrome P450 enzymes. *J. Phys. Chem. B* **2012**, *116* (1), 718−730.
(67) de Visser, S. P.; Shaik, S. A proton-shuttle mechanism mediated by the porphyrin in benzene hydroxylation by cytochrome P450 enzymes. *J. Am. Chem. Soc.* **2003**, *125* (24), 7413−7424.
(68) Bathelt, C. M.; Ridder, L.; Mulholland, A. J.; Harvey, J. N. Mechanism and structure−reactivity relationships for aromatic hydroxylation by cytochrome P450. *Org. Biomol. Chem.* **2004**, *2* (20), 2998−3005.
(69) Shaik, S.; Cohen, S.; Wang, Y.; Chen, H.; Kumar, D.; Thiel, W. P450 enzymes: their structure, reactivity, and selectivity—modeled by QM/MM calculations. *Chem. Rev.* **2010**, *110* (2), 949−1017.
(70) Altun, A.; Shaik, S.; Thiel, W. What is the active species of cytochrome P450 during camphor hydroxylation? QM/MM studies of different electronic states of compound I and of reduced and oxidized iron−oxo intermediates. *J. Am. Chem. Soc.* **2007**, *129* (29), 8978−8987.
(71) Krzystek, J.; England, J.; Ray, K.; Ozarowski, A.; Smirnov, D.; Que, L., Jr.; Telser, J. Determination by high-frequency and -field EPR of zero-field splitting in iron(IV) oxo complexes: implications for

https://doi.org/10.1021/acs.est.5c10288
Environ. Sci. Technol. 2026, 60, 2728−2741

intermediates in nonheme iron enzymes. *Inorg. Chem.* **2008**, *47* (9), 3483−3485.
(72) Shaik, S.; Chen, H.; Janardanan, D. Exchange-enhanced reactivity in bond activation by metal−oxo enzymes and synthetic reagents. *Nat. Chem.* **2011**, *3* (1), 19−27.

https://doi.org/10.1021/acs.est.5c10288
Environ. Sci. Technol. 2026, 60, 2728−2741